ISSN (Print) 1226-1750
ISSN (Online) 2233-6656
Journal of Magnetics 27(1), 1-6 (2022) https://doi.org/10.4283/JMAG.2022.27.1.001

Comparison of Spin Seebeck Signal in $Y_3Fe_5O_{12}$ Film Measured by Joule Heating- and Laser Heating-based Measurement Systems

Phuoc Cao Van[1†], Duc Duong Viet[1†], Trinh Nguyen Thi[1], Ji-Hwan Seol[1], Gun-Woo Park[1], Jong-Ryul Jeong[1]*, Seung-Young Park[2], and Churl Hee Cho[3]*

[1]*Department of Material Science and Engineering, Chungnam National University, Daejeon 34134, Republic of Korea*
[2]*Center for Scientific Instrumentation, Korea Basic Science Institute, Daejeon 34133, Republic of Korea*
[3]*Graduate School of Energy Science and Technology, Chungnam National University, Daejeon 34134, Republic of Korea*

(Received 8 November 2021, Received in final form 21 January 2022, Accepted 24 January 2022)

In this study, spin Seebeck effect (SSE) signals caused by a thermal gradient induced by Joule and laser heating were examined. A Pt/$Y_3Fe_5O_{12}$/$Gd_3Ga_5O_{12}$ sample was used as the reference for SSE measurement. Both the Joule heating- and laser heating-based SSE measurement systems captured SSE hysteresis loops consistent with the magnetic hysteresis loop of the sample. The laser heating-based system measured a higher SSE signal; however, heat flux could not be precisely evaluated. With the Joule heating-based system, the spin Seebeck resistivity (SSR) was 21.2 ± 1 nm/A, comparable with the values obtained in other studies and indicating the feasibility of our apparatus for investigating SSE.

Keywords : Spin Seebeck effect, spin Seebeck resistivity, Joule heating, laser heating, $Y_3Fe_5O_{12}$

1. Introduction

Recently, the spin Seebeck effect (SSE), a spin counterpart of the charge Seebeck effect (CSE), has been demonstrated experimentally [1]. The SSE refers to the generation of spin voltage *via* a thermal gradient, as a counterpart to electric voltage in the case of CSE; therefore, insulators can exhibit SSE, despite the absence of electrons [2]. Interesting studies on insulator spintronics have been conducted, and potential applications have been developed [3]. Specifically, magnetic spin dynamics have been studied based on the pure spin current from SSE [4, 5]. Moreover, spin thermoelectric devices can be manufactured based on the conversion of spin to electric voltage through the inverse spin Hall effect (ISHE) in the spin detection layer (SDL), which is placed adjacent to the spin source material [6-9]. The efficiency of these devices, which is directly proportional to the spin Hall angle (θ_{SH}) of the SDL, is below that of conventional thermoelectric devices [9-11]; however, using materials with extremely large θ_{SH}, such as topological insulators and Weyl semimetals, can improve device efficiency [12-16]. Furthermore, SSE-based devices have a layer-to-layer structure, which is much simpler than the structures of junction modules in CSE-based devices [7, 11]. This allows for much easier and low-cost manufacturing of spin thermoelectric devices, because the constituent materials can be fabricated *via* convenient industrial techniques such as spin coating and sputtering [11, 17, 18].

The electric voltage generated from longitudinal SSE is at the heart of spin thermoelectric devices. Its amplitude depends not only on θ_{SH}, but also on the interface quality of materials and the device dimensions [19-21]. The magnitude of SSE voltage (V_{SSE}) corresponding to a temperature difference of 1 Kelvin does not provide an eigenvalue for weighting the SSE response, because this value does not include the dimensional parameters [7, 22]; therefore, to evaluate the strength of SSE in a specific system, the spin Seebeck coefficient, which accounts for all of the above parameters, is first used. It is defined as $S_{SSE} = \frac{-E_{ISHE}}{\nabla T}$ (unit = V/K), where E_{ISHE} is the electric field induced by ISHE, and ∇T is the thermal gradient across the sample [20]. Here, E_{ISHE} is calculated from V_{SSE}/L_x (L_x is the length of the sample along the x-axis), and ∇T is obtained as $\Delta T/t$, where ΔT is the temperature difference between the top and bottom surfaces

†These authors contributed equally to this work

*Corresponding author: Tel: +82-42-821-7644
Fax: +82-42-833-3206, e-mail: jrjeong@cnu.ac.kr
e-mail: choch@cnu.ac.kr

of the sample, and t is the thickness between the surfaces. However, the ∇T estimated using the temperature difference method is usually incorrect because of the effect of the thermal resistance of contacts, *i.e.*, substrate and hot/cold reservoirs [23, 24]. Therefore, recent studies used heat flux to avoid uncertainty about the temperature gradient inside the film [25, 26]. Heat flux can be reliably obtained by normalizing heater power (P_{heater}) to the area of sample (A). The spin Seebeck coefficient obtained from the heat flux method is called spin Seebeck resistivity (SSR) of which amplitude is denoted as R_{SSE}.

$$R_{SSE} = \frac{E_{ISHE}}{j_Q} = \frac{E_{ISHE}/L_x}{P_{heater}/A} \text{ (unit = m/A)} \quad (1)$$

In the SSE measurement system, heat can be generated through several methods, among which Joule and laser heating have been widely used [17, 20, 27-31]. In the current work, we compare SSE measurement results obtained using Joule heating- and laser heating-based systems, and describe the strengths and weaknesses of each system. Moreover, from the result of the Joule heating-based SSE measurement system, we calculate the SSR of a Pt/$Y_3Fe_5O_{12}$/$Gd_3Ga_5O_{12}$ (Pt/YIG/GGG) sample, which is used for evaluating SSE efficiency.

2. Experimental Procedure

Figure 1 shows a simplified schematic of our Joule heating apparatus. The structure of the sample and its installation together with other components will be described later. The XZ stage was connected to a sample holder made of non-magnetic material. This stage enabled the sample position to be manually adjusted along the x and z directions, to centralize the sample relative to the external magnetic field. Stage movement could also be controlled using a motion controller with micrometer-scale accuracy. The magnetic field was created using several Helmholtz coils electrified by a bipolar DC power supplier. The real-time strength of the magnetic field was measured using a gauss meter, whose probe was placed near the sample loading position. The source meter supplied electric current to a 240-Ω resistive heater, which generated thermal gradient across the sample. The heater is a rectangular wave-like pattern made of steel and operated based on the Joule heating effect. The ISHE voltage (V_{ISHE}) was obtained using a nano-voltmeter (2182A; Keithley) through gold (Au) wiring connections. All electric components were connected to a personal computer *via* general-purpose interface bus cables. LabVIEW was used to control and receive measurement data from the devices. In laser system, except for the thermal source equipment, *i.e.*, laser, most of the electrical equipment are the same with Joule heating system. To generate a sufficient temperature gradient, laser light is focused into 5 μm in diameter to increase the light density. Besides, Pt is patterned into a 1 mm × 10 μm line to achieve a detectable SSE voltage. Without the patterning Pt into the micrometer scale, there is no SSE signal detection with our laser system. This could be attributed to the low density of our laser source and thin Pt film (5 nm) of which absorption rate is also low. To solve this problem, Wang *et al.* covered an absorbing layer on Pt to increase the light absorption [28]. However, this requires an additional process which makes sample fabrication complicated. The laser light is aligned *via* a microscale motion controller to shine on the center of the Pt pattern in the direction which is normal to the sample plane. All of the systems are set up on a vibration isolation table to prevent the displacement of the components.

The sample installation of the laser system can be found in our previous report [17] while that of the Joule heating system is depicted in Fig. 2(a). The sample consists of Pt pattern and Au electrical contact pads (see the detail in the sample fabrication) was loaded on a copper heat sink placed on the sample holder (Fig. 1). Then, a resistive heater was attached to the surface of the Pt pattern through a beryllium oxide (BeO) plate using thermal grease to ensure heat flux. Owing to its high thermal conductivity, BeO ensures uniform diffusion of heat from the heater to the Pt layer. At the bottom surface of the sample (*i.e.*, the GGG surface), a thin thermal grease layer was also applied to ensure contact between the sample and heat sink. The V_{ISHE} induced in the Pt layer was measured using a nano-voltmeter connected to Au pads by silver paste. Then, we examined the heater performance under varying electric current amplitudes corresponding to the

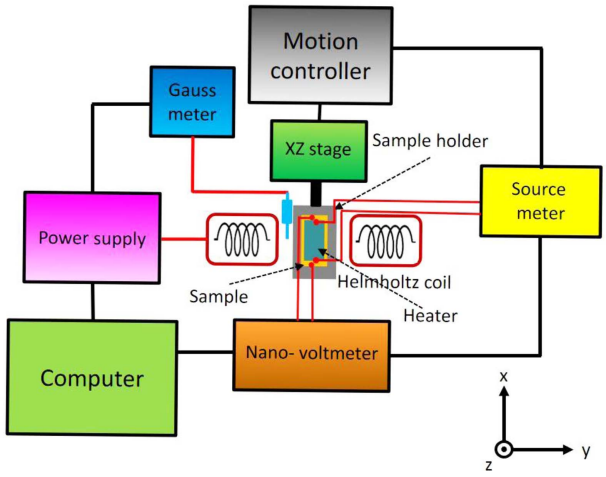

Fig. 1. (Color online) Schematic of the Joule heating-based SSE measurement system.

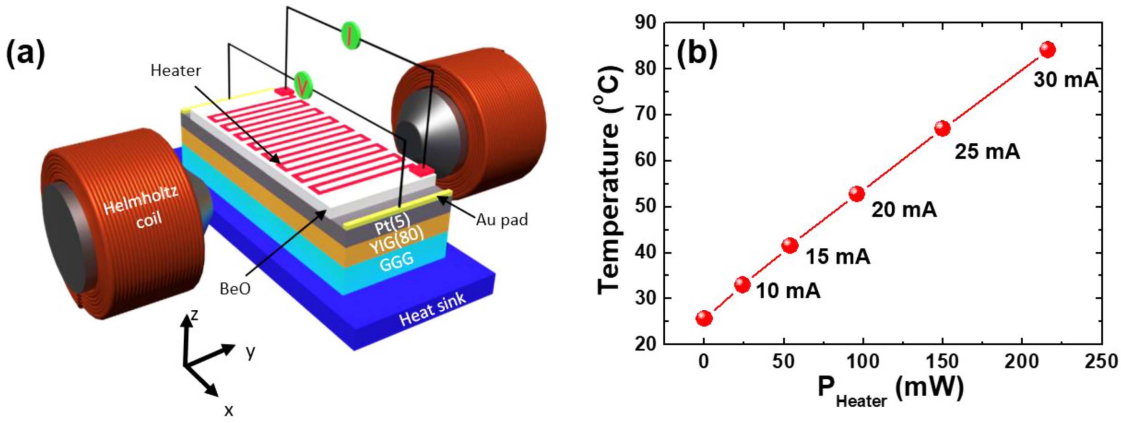

Fig. 2. (Color online) (a) Illustration of sample installation for SSE measurement, the unit of number in bracket is nanometer; (b) plot of temperature as a function of P_{heater}.

supplied power. The heater temperature was measured using a Pt resistance thermometer (Pt100), and temperature was plotted as a function of P_{heater} (Fig. 2(b)). The temperature linearly increased with power, indicating good condition of the heater.

To evaluate the performance of our measurement systems, we prepared the Pt(5)/YIG(80)/GGG (unit = nm) sample for SSE measurement. First, amorphous YIG films were ablated from a polycrystalline target, which was prepared *via* a solid-state reaction of a Fe_2O_3 and Y_2O_3 mixture. The target mixture was sieved twice and calcinated at 1,200 °C for 6 h. Then, it was pelleted in a mold *via* cold isostatic pressing at 2,000 kg/cm^2. Subsequently, the pellet was sintered at 1,350 °C under air, and then ground to 2-in. diameter and 4-mm thickness for use as the sputtering target. Furthermore, 111-oriented GGG substrate was used to ensure epitaxial growth of YIG, because its lattice constant is close to that of YIG [18]. Before sputtering, the substrate was sonicated in acetone, isopropanol, and ethanol to remove impurities on its surface. The sputtering chamber was evacuated below 8×10^{-7} Torr, and the substrate temperature was elevated to 300 °C. The film was deposited at a power of 100 W; constant pressure, with argon and oxygen injection flow rates of

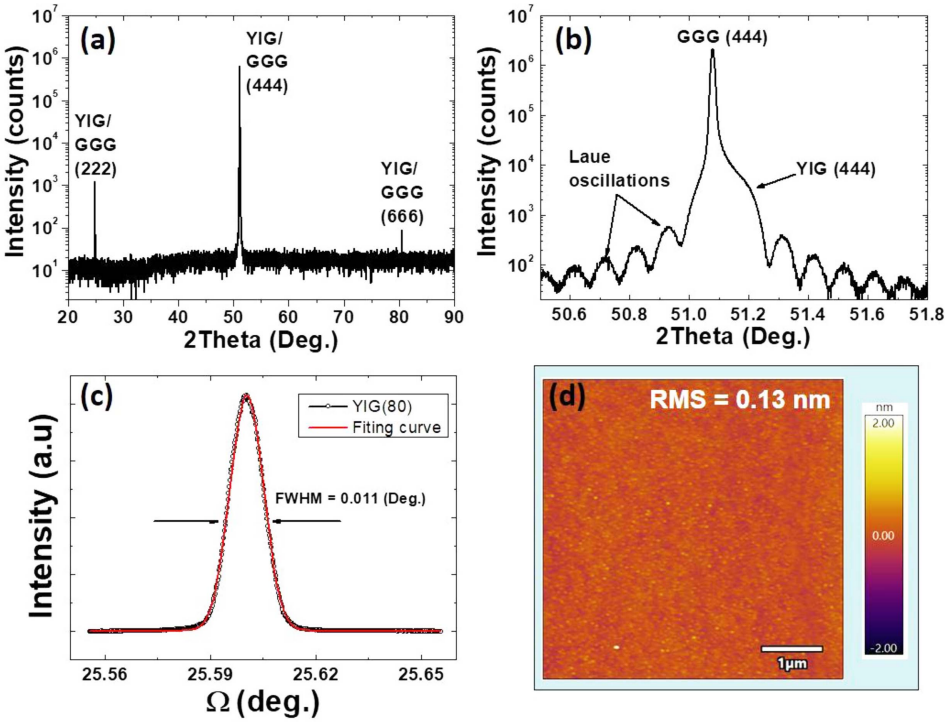

Fig. 3. (Color online) (a) Wide, (b) narrow, and (c) rocking curve XRD scans; (d) surface morphology of the YIG/GGG sample.

22.5 and 2.5 sccm, respectively. To crystallize YIG, the amorphous film was annealed at 850 °C in an oxygen-rich environment for 2 h, with heating and cooling rates of 4 °C/min and 2 °C/min, respectively. Then, the surface of the annealed sample was cleaned with argon plasma. For measurement with the Joule heating system, a 5-nm Pt layer as the SDL was deposited on the YIG/GGG sample in a DC sputtering chamber using a shadow mask, to form a 6 × 2 mm pattern. Finally, a pair of 100-nm Au contact pads was deposited on two heads of the Pt pattern along the 2-mm side. For measurement using the laser heating system, Pt layer was patterned into a 1 mm × 10 μm line *via* photolithography and ion milling.

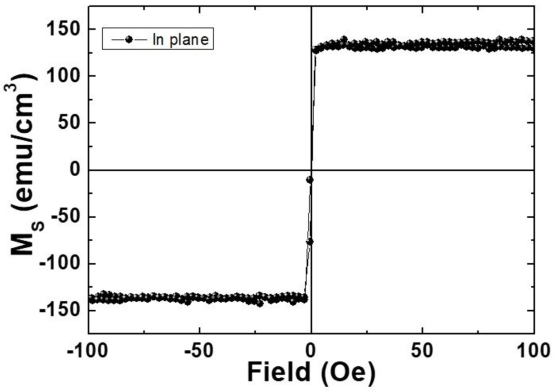

Fig. 4. In-plane magnetic hysteresis loop of YIG(80)/GGG.

3. Results and Discussion

To confirm the quality of the YIG sample, we investigated its crystallinity, surface morphology and magnetic properties. Fig. 3(a) shows a Ω/2θ wide scan of the X-ray diffraction (XRD) spectra of the YIG(80)/GGG sample. The spectra showed no secondary phase peak, indicating that the YIG film had a single-crystal structure. The XRD scan of the region surrounding the YIG/GGG(444) diffraction peak is shown in Fig. 3(b). The larger diffraction angle indicates a slightly smaller lattice constant of YIG compared with GGG. Moreover, the spectra showed Laue fringes, indicating epitaxial growth of YIG film. Fig. 3(c) presents the rocking curve scan, which showed a full width at half maximum of 0.011°, demonstrating good crystallographic texture of the film without mosaicity. Fig. 3(d) shows the atomic force microscopy spectra of the sample. The root-mean-square roughness was 0.13 nm, which reflects the smooth surface of the YIG film. The XRD and atomic force microscopy results confirm the good crystallization of YIG under the annealing process. Finally, we measured the magnetic properties of the sample *via* vibrating-sample magnetometry (Fig. 4). A hysteresis loop was obtained under a sweeping field of −100 to100 Oe, which was sufficient to saturate the film. The paramagnetic signal from the GGG substrate was

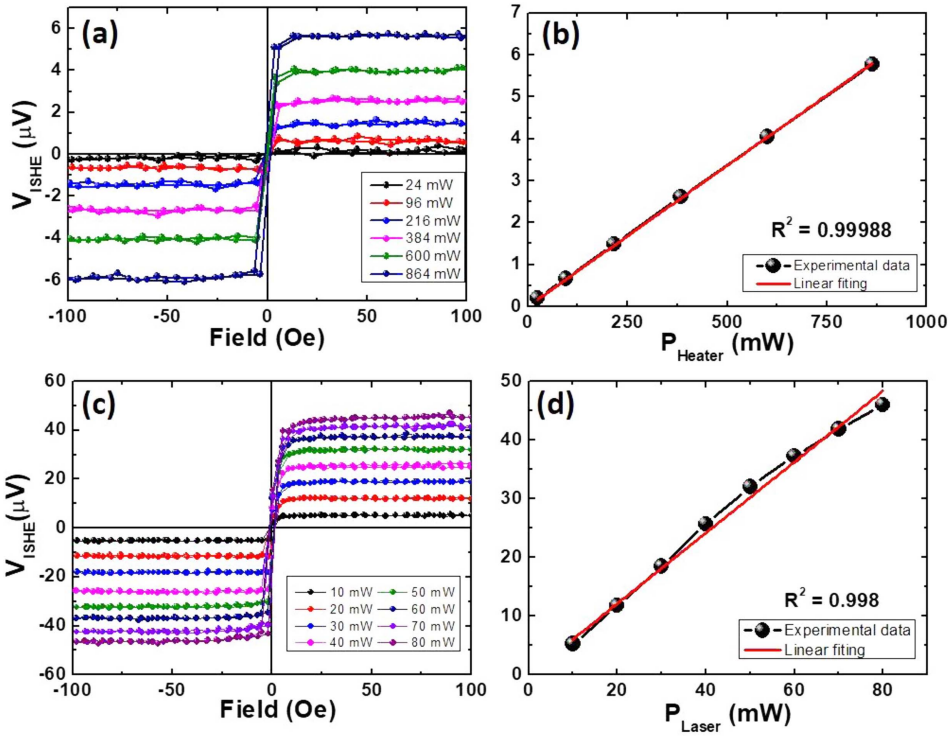

Fig. 5. (Color online) (a) V_{ISHE} data obtained through SSE measurement using the Joule heating system; (b) V_{ISHE} as a function of P_{heater}; (c) V_{ISHE} data obtained through SSE measurement using the laser heating system; (d) V_{ISHE} as a function of P_{laser}.

subtracted from the measured curve. The saturation magnetization value, which was obtained by dividing the magnetic moment by the volume of the sample, was approximately 135 ± 2 Oe; this value is slightly lower than the theoretical bulk value but comparable to those of other films prepared using the same technique [32, 33]. The coercivity of the sample was very small, almost approaching zero, reaffirming the outstanding quality of our sputtered YIG film.

Then, SSE measurements were performed at ambient temperature for the Joule heating and laser heating systems (Fig. 5(a) and (c), respectively). The V_{ISHE} hysteresis loops were obtained *via* an external magnetic field sweep. The loops had almost the same shape as those measured by vibrating-sample magnetometry, proving that the signal originated from SSE. We extracted V_{ISHE} as a function of P_{heater} and laser power (P_{laser}) (Fig. 5(c) and (d), respectively), and the data were fitted to a linear equation (red line in the graphs). The results of both systems show linear dependence of V_{ISHE} on heat source power, indicating good performance of our systems, consistent with the data. However, the Joule heating system has a better coefficient of determination (R^2), presumably because of the effect of the power laser controller. The amplitude of V_{ISHE} during laser heating is approximately 1 order of magnitude larger than that in the Joule heating system. For unbiased comparison, V_{ISHE} needs to be normalized to the dimension factor and power of the heat source. Here, we do not mention the real power absorbed in the Pt layer, but rather the supplied power of the device. The normalization result can be considered as the primary output efficiency (ξ_P) of each system. Specifically, $\xi_P = \frac{V_{ISHE}}{P.R}$ where P is supplied power of laser and heater and R is the resistance of the sample. Since the Pt thicknesses in the two cases are the same, the resistance of the sample depends on the dimensions of the Pt pattern. Using the two-probe method, the resistances of samples used in Joule and laser heating systems were obtained as 0.7 and 20.3 kΩ, respectively; these values are consistent with the $\frac{L}{A}$ ratios of the Pt patterns: $\frac{1}{3}$ and $\frac{1}{100}$ for the Joule and laser heating-based systems, respectively (see device dimensions in section II). The resistance of a conducting body is defined as $R = \rho\frac{L}{A}$, where ρ, L, and A are the resistivity, length, and area of the sample, respectively. Moreover, both systems have the same material and thus the same ρ; therefore, the resistance ratio is almost proportional to the ratio of $\frac{L}{A}$. The ξ_P values of the Joule heating and laser heating systems are calculated as $9.54 \pm 0.01 \times 10^{-3}$ and $28.3 \pm 0.2 \times 10^{-3}$ $\frac{\mu V}{k\Omega.mW}$, respectively, indicating that the laser heating system outperformed the Joule heating system in terms of obtaining a high SSE signal. However, preparing the samples and aligning them for laser spots during measurements are complicated processes. Moreover, in the case of the laser heating system, the heat flux and R_{SSE} cannot be precisely defined because of unknown power absorption in the Pt layer. As for the Joule heating system, the power supplied to the Pt layer equals the P_{heater} and thus the heat flux, and can be easily calculated. From the V_{ISHE} data, we determine the SSR of our sample for the Joule heating system using eq. (1); the obtained value is 21.2 ± 1 nm/A, comparable to that previously reported for the same sample structure [26]. This result confirms the reliability of our SSE measurement system, which has simple sample preparation and installation processes.

4. Conclusion

We measured the SSE of a Pt/YIG/GGG sample at room temperature using two measurement systems; the thermal gradient was excited by the Joule heating effect in one system and the laser heating effect in the other. Both systems provided reasonable V_{SSE} data, consistent with the magnetic properties of the sample. The laser heating system presented a higher signal, but R_{SSE} was undefined. The R_{SSE} measured using the Joule heating system agreed with those of other systems, confirming the reliability of the system.

Acknowledgments

This work was supported by Chungnam National University.

References

[1] K. Uchida, S. Takahashi, K. Harii, J. Ieda, W. Koshibae, K. Ando, S. Maekawa, and E. Saitoh, Nature **455**, 778 (2008).

[2] K. Uchida, J. Xiao, H. Adachi, J. Ohe, S. Takahashi, J. Ieda, T. Ota, Y. Kajiwara, H. Umezawa, H. Kawai, G.E.W. Bauer, S. Maekawa, and E. Saitoh, Nat. Mater. **9**, 894 (2010).

[3] A. Hirohata, K. Yamada, Y. Nakatani, L. Prejbeanu, B. Diény, P. Pirro, and B. Hillebrands, J. Magn. Magn. Mater. **509**, 166711 (2020).

[4] J. Barker, G. E. W. Bauer, Phys. Rev. Lett. **117**, 217201 (2016).

[5] T. S. Seifert, S. Jaiswal, J. Barker, S. T. Weber, I. Razdolski, J. Cramer, O. Gueckstock, S. F. Maehrlein, L. Nadvornik, S. Watanabe, C. Ciccarelli, A. Melnikov, G. Jakob, M. Münzenberg, S. T. B. Goennenwein, G. Woltersdorf, B. Rethfeld, P. W. Brouwer, M. Wolf, M. Kläui,

and T. Kampfrath, Nat. Commun. **9**, 2899 (2018).
[6] J.-M. Kim, C.-Y. Jeon, D.-J. Kim, P. Cao Van, J.-R. Jeong, and B.-G. Park, ACS Appl. Electron. Mater. **2**, 2906 (2020).
[7] A. Kirihara, K. I. Uchida, Y. Kajiwara, M. Ishida, Y. Nakamura, T. Manako, E. Saitoh, and S. Yorozu, Nat. Mater. **11**, 686 (2012).
[8] A. B. Cahaya, O. A. Tretiakov, and G. E. W. Bauer, IEEE Trans. Magn. **51**, 0800414 (2015).
[9] M. Y. Kim, S. J. Park, G. Y. Kim, S. Y. Choi, and H. Jin, Energy Environ. Sci. **14**, 3480 (2021).
[10] A. B. Cahaya, O. A. Tretiakov, and G. E. W. Bauer, Appl. Phys. Lett. **104**, 042402 (2014).
[11] K. I. Uchida, H. Adachi, T. Kikkawa, A. Kirihara, M. Ishida, S. Yorozu, S. Maekawa, and E. Saitoh, Proc. IEEE. **104**, 1946 (2016).
[12] Z. Jiang, C. Z. Chang, M. R. Masir, C. Tang, Y. Xu, J. S. Moodera, A. H. Macdonald, and J. Shi, Nat. Commun. **7**, 11458 (2016).
[13] B. Zhao, D. Khokhriakov, Y. Zhang, H. Fu, B. Karpiak, A. Md. Hoque, X. Xu, Y. Jiang, B. Yan, and S. P. Dash, Phys. Rev. Res. **2**, 013286 (2020).
[14] N. H. D. Khang, Y. Ueda, and P. N. Hai, Nat. Mater. **17**, 808 (2018).
[15] N. H. D. Khang, S. Nakano, T. Shirokura, Y. Miyamoto, and P. N. Hai, Sci. Rep. **10**, 12185 (2020).
[16] T. Fan, N. H. D. Khang, T. Shirokura, H. H. Huy, and P. N. Hai, Appl. Phys. Lett. **119**, 082403 (2021).
[17] T. N. Thi, P. C. Van, D. D. Viet, V. D. Quoc, H. Ahn, V. A. Cao, M. G. Kang, J. Nah, B. G. Park, and J. R. Jeong, Ceram. Int. **47**, 16770 (2021).
[18] P. Cao Van, S. Surabhi, V. Dongquoc, R. Kuchi, S. G. Yoon, and J. R. Jeong, Appl. Surf. Sci. **435**, 377 (2018).
[19] T. Niimura, Y. Kurokawa, S. Horiike, H. Li, H. Hanamoto, R. Weber, A. Berger, and H. Yuasa, Phys. Rev. B. **102**, 94411 (2020).
[20] A. Sola, P. Bougiatioti, M. Kuepferling, D. Meier, G. Reiss, M. Pasquale, T. Kuschel, and V. Basso, Sci. Rep. **7**, 46752 (2017).
[21] K. Uchida, M. Ishida, T. Kikkawa, A. Kirihara, T. Murakami, and E. Saitoh, J. Phys. Condens. Matter. **26**, 343202 (2014).
[22] G. Siegel, M. C. Prestgard, S. Teng, and A. Tiwari, Sci. Rep. **4**, 4429 (2014).
[23] A. Sola, M. Kuepferling, V. Basso, M. Pasquale, T. Kikkawa, K. Uchida, and E. Saitoh, J. Appl. Phys. **117**, 17C510 (2015).
[24] A. Sola, V. Basso, M. Kuepferling, M. Pasquale, D. Meier, G. Reiss, T. Kuschel, T. Kikkawa, K. Uchida, E. Saitoh et al., IEEE Trans. Instrum. Meas. **68**, 1765 (2018).
[25] G. Venkat, T.A. Rose, C. D. W. Cox, G. B. G. Stenning, A. J. Caruana, and K. Morrison, Epl. **126**, 37001 (2019).
[26] A. Prakash, B. Flebus, J. Brangham, F. Yang, Y. Tserkovnyak, and J. P. Heremans, Phys. Rev. B. **97**, 020408(R) (2018).
[27] Y. J. Chen and S. Y. Huang, Phys. Rev. B. **99**, 94426 (2019).
[28] S. Wang, G. Li, J. Wang, H. Yan, and K. Jin, J. Magn. Magn. Mater. **468**, 50 (2018).
[29] M. U. Fayaz, M. S. Saleem, Y. Gu, X. Zhou, F. Pan, and C. Song, J. Appl. Phys. **126**, 183901 (2019).
[30] W. X. Wang, S. H. Wang, L. K. Zou, J. W. Cai, Z. G. Sun, and J. R. Sun, Appl. Phys. Lett. **105**, 182403 (2014).
[31] C. Y. Jeon, K. M. Baek, S. Kim, D. J. Kim, M. S. Jang, Y. S. Jung, and B. G. Park, Adv. Funct. Mater. **28**, 1802936 (2018).
[32] J. Ding, T. Liu, H. Chang, and M. Wu, IEEE Magn. Lett. **11**, 5502305 (2020).
[33] C. Hauser, T. Richter, N. Homonnay, C. Eisenschmidt, M. Qaid, H. Deniz, D. Hesse, M. Sawicki, S. G. Ebbinghaus, and G. Schmidt, Sci. Rep. **6**, 20827 (2016).